

Learning Deep Conditional Target Densities for Accurate Regression

Fredrik K. Gustafsson^{*,1}Martin Danelljan^{*,2}Goutam Bhat²Thomas B. Schön¹¹Department of Information Technology, Uppsala University, Sweden²Computer Vision Laboratory, ETH Zurich, Switzerland

Abstract

While deep learning-based classification is generally addressed using standardized approaches, a wide variety of techniques are employed for regression. In computer vision, one particularly popular such technique is that of confidence-based regression, which entails predicting a confidence value for each input-target pair (x, y) . While this approach has demonstrated impressive results, it requires important task-dependent design choices, and the predicted confidences lack a natural probabilistic meaning.

We address these issues by proposing a general and conceptually simple regression method with a clear probabilistic interpretation. In our proposed approach, we create an energy-based model of the conditional target density $p(y|x)$, using a deep neural network to predict the un-normalized density from (x, y) . This model of $p(y|x)$ is trained by directly minimizing the associated negative log-likelihood, approximated using Monte Carlo sampling. We perform comprehensive experiments on four computer vision regression tasks. Our approach outperforms direct regression, as well as other probabilistic and confidence-based methods. Notably, our model achieves a 1.9% AP improvement over Faster-RCNN for object detection on the COCO dataset, and sets a new state-of-the-art on visual tracking when applied for bounding box regression.

1. Introduction

Supervised regression entails learning a model capable of predicting a continuous target value y from an input x , given a set of paired training examples. It is a fundamental machine learning problem with many important applications within computer vision and other domains. Common regression tasks within computer vision include object detection [53, 27, 32, 68], head- and body-pose estimation [4, 62, 58, 64], age estimation [54, 47, 3], visual tracking [43, 69, 35, 8] and medical image registration [44, 5],

^{*}Both authors contributed equally.

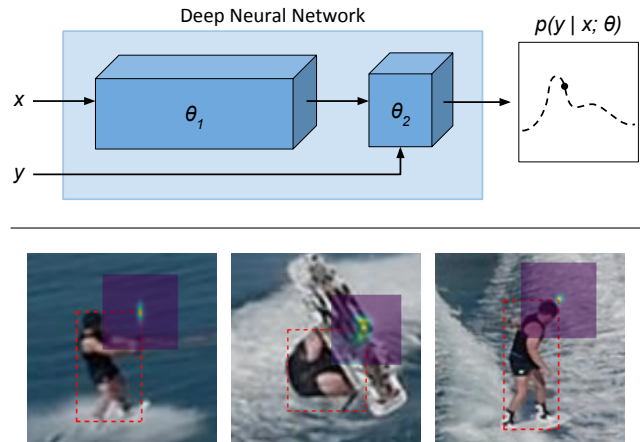


Figure 1: An overview of the proposed regression method (top). We train an energy-based model $p(y|x; \theta)$ of the conditional target density, using a deep neural network to predict the un-normalized density directly from the input-target pair (x, y) . Our approach is capable of predicting highly flexible densities. This is demonstrated for the problem of bounding box regression (bottom), visualizing the marginal density for the top right corner as a heatmap. Our model captures meaningful uncertainty, while achieving highly accurate estimates.

just to mention a few. While all of these tasks benefit from accurate regression of the target values, high accuracy can even be safety-critical in e.g. automotive and medical applications. Today, such regression problems are commonly tackled using Deep Neural Networks (DNNs), due to their ability to learn powerful feature representations from data.

While classification is generally addressed using standardized losses and output representations, a wide variety of different techniques are employed for regression. The most conventional strategy is to train a DNN to directly predict a target y given an input x [31]. In such *direct regression* approaches, the model parameters of the DNN are learned by minimizing a loss function, for example the L^2 or L^1 loss, penalizing discrepancy between the predicted and ground

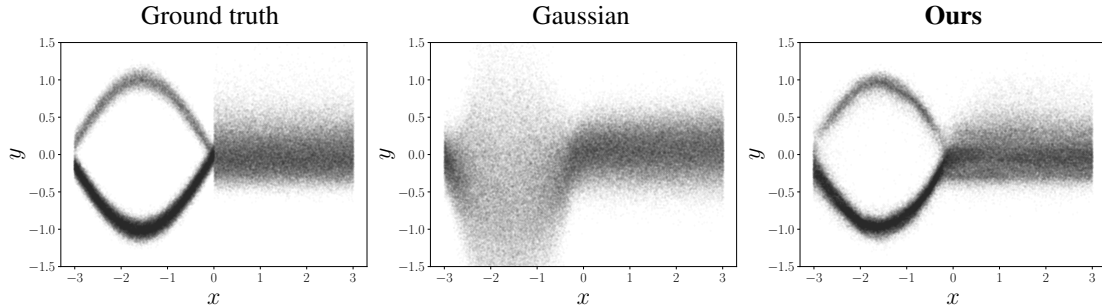


Figure 2: An illustrative 1D regression problem. The training data $\{(x_i, y_i)\}_{i=1}^{2000}$ is generated by the ground truth conditional target density $p(y|x)$. Our energy-based model $p(y|x; \theta) \propto e^{f_\theta(x, y)}$ of $p(y|x)$ is trained by directly minimizing the associated negative log-likelihood, approximated using Monte Carlo sampling. In contrast to the Gaussian model $p(y|x; \theta) = \mathcal{N}(y; \mu_\theta(x), \sigma_\theta^2(x))$, our model can learn complex conditional target densities directly from data.

truth target values. From a probabilistic perspective, this approach corresponds to creating a simple parametric model of the conditional target density $p(y|x)$, and minimizing the associated negative log-likelihood. The L^2 loss, for example, corresponds to a fixed-variance Gaussian model. More recent work [28, 30, 6, 17] has also explored learning more expressive models of $p(y|x)$, by letting a DNN instead output the full set of parameters of a certain family of probability distributions. These *probabilistic regression* approaches however restrict the parametric model to fairly simple distributions, such as Gaussian [30, 6] or Laplace [28, 17, 26], limiting the expressiveness of the learned conditional target density. While these methods benefit from a clear probabilistic interpretation, they thus fail to fully exploit the predictive power of the DNN.

The quest for improved regression accuracy has also led to the development of more specialized methods, designed for a specific set of tasks. In computer vision, one particularly popular approach is that of *confidence-based regression*. Here, a DNN instead predicts a scalar confidence value for input-target pairs (x, y) . The confidence can then be maximized w.r.t. y to obtain a target prediction for a given input x . This approach is commonly employed for image-coordinate regression tasks within e.g. human pose estimation [4, 62, 58] and object detection [32, 68], where a 2D heatmap over image pixel coordinates y is predicted. Recently, the approach was also applied to the problem of bounding box regression by Jiang et al. [27]. Their proposed method, IoU-Net, obtained state-of-the-art accuracy on object detection, and was later also successfully applied to the task of visual tracking [8]. The training of such confidence-based regression methods does however entail generating additional pseudo ground truth labels, by for example employing a Gaussian kernel [60, 62], and selecting an appropriate loss function. This both requires numerous design choices to be made, and limits the general applicability of the methods. Moreover, confidence-based regression methods do not allow for a natural probabilistic interpreta-

tion in terms of the conditional target density $p(y|x)$. In this work, we therefore set out to develop a method combining the general applicability and clear interpretation of probabilistic regression with the predictive power of confidence-based approaches.

Contributions We propose a general and conceptually simple regression method with a clear probabilistic interpretation. Our proposed method employs an energy-based model [34] to predict the un-normalized conditional target density $p(y|x)$ from the input-target pair (x, y) . It is trained by directly minimizing the associated negative log-likelihood by exploiting Monte Carlo approximations. At test time, targets are predicted by maximizing the conditional target density $p(y|x)$ through gradient-based refinement. Compared to confidence-based approaches, our method requires no pseudo labels and benefits from a direct probabilistic interpretation. Unlike commonly used probabilistic models, our approach can learn highly flexible target densities directly from data, as visualized in Figure 2.

We evaluate the proposed method on four diverse computer vision regression tasks: object detection, visual tracking, age estimation and head-pose estimation. Our method is found to outperform both the direct regression baselines, and popular probabilistic and confidence-based alternatives. Notably, our method achieves a 1.9% AP improvement over the FPN Faster-RCNN [36] baseline on the COCO dataset [37] when applied for object detection. It also sets a new state-of-the-art on standard benchmarks [41, 42] when applied for bounding box regression in the recent ATOM [8] visual tracking algorithm.

2. Background & related work

In supervised regression, the task is to learn to predict a target value $y^* \in \mathcal{Y}$ from a corresponding input $x^* \in \mathcal{X}$, given a training set of i.i.d. input-target examples, $\mathcal{D} = \{(x_i, y_i)\}_{i=1}^N$, $(x_i, y_i) \sim p(x, y)$. As opposed

to classification, the target space \mathcal{Y} is a continuous set, e.g. $\mathcal{Y} = \mathbb{R}^K$. In computer vision, the input space \mathcal{X} often corresponds to the space of images, whereas the output space \mathcal{Y} depends on the task at hand. Common examples include $\mathcal{Y} = \mathbb{R}^2$ in image-coordinate regression [62, 32], $\mathcal{Y} = \mathbb{R}_+$ in age estimation [54, 47], and $\mathcal{Y} = \mathbb{R}^4$ in object bounding box regression [53, 27].

Direct regression Over the last decade, DNNs have been shown to excel at a variety of regression problems. Here, a DNN is viewed as a function $f_\theta : \mathcal{U} \rightarrow \mathcal{O}$, parameterized by a set of learnable weights $\theta \in \mathbb{R}^P$. The most conventional regression approach is to train a DNN to directly predict the targets, $y^* = f_\theta(x^*)$, called *direct regression*. The model parameters θ are learned by minimizing a loss $\ell(f_\theta(x_i), y_i)$ that penalizes discrepancy between the prediction $f_\theta(x_i)$ and the ground truth target value y_i on training samples (x_i, y_i) . The most common choices are the L^2 loss, $\ell(\hat{y}, y) = \|\hat{y} - y\|_2^2$, the L^1 loss, $\ell(\hat{y}, y) = \|\hat{y} - y\|_1$, and their close relatives [25, 31]. From a probabilistic perspective, the choice of loss corresponds to minimizing the negative log-likelihood $-\log p(y|x; \theta)$ of a specific model $p(y|x; \theta)$ of the conditional target density. For example, the L^2 loss is derived from a fixed-variance Gaussian model, $p(y|x; \theta) = \mathcal{N}(y; f_\theta(x), \sigma^2)$.

Probabilistic regression More recent work [28, 30, 6, 17, 26] has explicitly taken advantage of this probabilistic perspective to achieve more flexible parametric models $p(y|x; \theta) = p(y; \phi_\theta(x))$, by letting the DNN output the parameters ϕ of a family of probability distributions $p(y; \phi)$. For example, a general 1D Gaussian model can be realized as $p(y|x; \theta) = \mathcal{N}(y; \mu_\theta(x), \sigma_\theta^2(x))$, where the DNN outputs the mean and log-variance as $f_\theta(x) = \phi_\theta(x) = [\mu_\theta(x) \quad \log \sigma_\theta^2(x)]^\top \in \mathbb{R}^2$. The model parameters θ are learned by minimizing the negative log-likelihood $-\sum_{i=1}^N \log p(y_i|x_i; \theta)$ over the training set \mathcal{D} . At test time, a target estimate y^* is obtained by first predicting the density parameter values $\phi_\theta(x^*)$ and then, for instance, taking the expected value of $p(y; \phi_\theta(x))$. Previous work has applied Gaussian and Laplace models on computer vision tasks such as object detection [14, 22] and optical flow estimation [17, 26]. The aim of such probabilistic approaches is often not only to achieve accurate predictions, but also to provide an estimate of the aleatoric uncertainty [28], which models noise and ambiguities inherent in the data itself. Our proposed method also entails predicting a conditional target density $p(y|x; \theta)$ and minimizing the associated negative log-likelihood. However, our energy-based model $p(y|x; \theta)$ is not restricted to the functional form of any specific probability density (e.g. Gaussian or Laplace), but is instead directly defined by the DNN architecture itself, allowing for more expressive target densities.

Confidence-based regression Another category of ap-

proaches reformulates the regression problem as $y^* = \arg \max_y f_\theta(x, y)$, where $f_\theta(x, y) \in \mathbb{R}$ is a scalar confidence value predicted by the DNN. The idea is thus to predict a quantity $f_\theta(x, y)$, depending on both input x and target y , that can be maximized over y to obtain the final prediction y^* . This maximization-based formulation is inherent in Structural SVMs [59], but has also been adopted for DNNs. We term this family of approaches *confidence-based regression*. Different from direct regression, the predicted confidence $f_\theta(x, y)$ can encapsulate multiple hypotheses and other ambiguities. Confidence-based regression has been shown particularly suitable for image-coordinate regression tasks, such as hand keypoint localization [57] and body-part detection [60, 49, 62]. In these cases, a CNN is trained to output a 2D heatmap over the image pixel coordinates y , thus taking full advantage of the translational invariance of the problem. A similar approach has also been employed to locate the two defining corners [32] or four extreme points [68] of bounding boxes in object detection. In computer vision, confidence prediction has also been successfully employed for tasks other than pure image-coordinate regression. Jiang et al. [27] proposed the IoU-Net for bounding box regression in object detection, where a bounding box $y \in \mathbb{R}^4$ and image x are both input to the DNN to predict a confidence $f_\theta(x, y)$. It employs a pooling-based architecture that is differentiable w.r.t. the bounding box y , allowing efficient gradient-based maximization to obtain the final estimate $y^* = \arg \max_y f_\theta(x, y)$. IoU-Net was later also successfully applied to visual tracking [8].

In general, confidence-based approaches are trained using a set of *pseudo label* confidences $c(x_i, y_i, y)$ generated for each training example (x_i, y_i) , and by employing a loss $\ell(f_\theta(x_i, y), c(x_i, y_i, y))$. One strategy [49, 32] is to treat the confidence prediction as a binary classification problem, where $c(x_i, y_i, y)$ represents either the class, $c \in \{0, 1\}$, or its probability, $c \in [0, 1]$, and employ cross-entropy based losses ℓ . The other approach is to treat the confidence prediction as a direct regression problem itself by applying standard regression losses, such as L^2 [57, 8, 60] or the Huber loss [27]. In these cases, the pseudo label confidences c can be constructed using a similarity measure S in the target space, $c(x_i, y_i, y) = S(y, y_i)$, for example defined as the Intersection over Union (IoU) between two bounding boxes [27] or simply by a Gaussian kernel [60, 62, 58]. While these methods have demonstrated impressive results, existing confidence-based approaches require important design choices. In particular, the strategy for constructing the pseudo labels c and the choice of loss ℓ are often crucial for performance and highly task-dependent. Moreover, the predicted confidence $f_\theta(x, y)$ can be difficult to interpret, since it has no natural connection to the conditional target density $p(y|x)$. In contrast, our approach is directly trained to predict $p(y|x)$ itself, and does not require generation of

pseudo label confidences or choosing a specific loss.

Regression-by-classification A regression problem can also be treated as a classification problem by first discretizing the target space \mathcal{Y} into a finite set of C classes. Standard techniques from classification, such as softmax and the cross-entropy loss, can then be employed. Rothe et al. [54] additionally computed the softmax expected value to obtain a more fine-grained prediction, and applied their method to the task of age estimation. Ruiz et al. [55] applied the same method to head-pose estimation, but also added an L^2 loss term for the softmax expected value during training. Again for age estimation, Pan et al. [47] then added an additional loss term penalizing the softmax variance. A hierarchical classification approach has also been proposed for both age estimation [65] and head-pose estimation [64]. The discretization of the target space \mathcal{Y} often complicates exploiting its inherent neighborhood structure. This has been addressed by exploring ordinal regression methods for 1D problems [3, 10]. Finally, classification into coarse discrete bins can be combined with direct regression, a technique often utilized in 2D [51, 38] and 3D [56, 50] object detection. While our energy-based approach can be seen as a generalization of the softmax model for classification to the continuous target space \mathcal{Y} , it does not suffer from the aforementioned drawbacks of regression-by-classification. On the contrary, our model naturally allows the network to exploit the full structure of the continuous target space \mathcal{Y} .

Energy-based models Our approach is related to the theoretical framework of energy-based models, which often has been employed for machine learning problems in the past [40, 23, 34]. It involves learning an energy function $\mathcal{E}_\theta(x) \in \mathbb{R}$ that assigns low energy values to observed data x_i and high energies to other values of x . In recent years, energy-based models have been used primarily for unsupervised learning problems within computer vision [63, 16, 11, 33, 45], where DNNs are directly used to predict the energy function $\mathcal{E}_\theta(x)$. These models are commonly trained by minimizing the negative log-likelihood, stemming from the probabilistic model $p(x; \theta) = e^{-\mathcal{E}_\theta(x)} / \int e^{-\mathcal{E}_\theta(x)} dx$, for example by generating approximate image samples from $p(x; \theta)$ using Markov Chain Monte Carlo methods [16, 11, 45]. In contrast, we employ an energy-based representation of $p(y|x)$ in the supervised regression setting, and apply it to fundamental computer vision problems such as object detection and pose estimation, where the target space \mathcal{Y} is low-dimensional.

3. Proposed regression method

We propose a general regression method with a clear probabilistic interpretation. The approach is formulated in Section 3.1. In Section 3.2, we introduce a sampling-based training strategy, designed to be practically applicable to

common regression tasks within computer vision. Lastly, we discuss inference strategies in Section 3.3.

3.1. Formulation

We take the probabilistic view of regression by creating a model $p(y|x; \theta)$ of the conditional target density $p(y|x)$, in which θ is learned by minimizing the associated negative log-likelihood. Instead of defining $p(y|x; \theta)$ by letting a DNN predict the parameters of a certain family of probability distributions (e.g. Gaussian or Laplace), we construct a versatile energy-based model that can better leverage the predictive power of DNNs. To that end, we take inspiration from confidence-based regression approaches and let a DNN directly predict a scalar value for any input-target pair (x, y) . Unlike confidence-based methods however, this prediction has a clear probabilistic interpretation. Specifically, we view a DNN as a function $f_\theta : \mathcal{X} \times \mathcal{Y} \rightarrow \mathbb{R}$, parameterized by $\theta \in \mathbb{R}^P$, that maps an input-target pair $(x, y) \in \mathcal{X} \times \mathcal{Y}$ to a scalar value $f_\theta(x, y) \in \mathbb{R}$. Then, we define our model $p(y|x; \theta)$ according to,

$$p(y|x; \theta) = \frac{e^{f_\theta(x, y)}}{Z(x, \theta)}, \quad Z(x, \theta) = \int e^{f_\theta(x, y)} dy, \quad (1)$$

where $Z(x, \theta)$ is the normalizing partition function. We train this energy-based model $p(y|x; \theta)$ by directly minimizing the negative log-likelihood $-\log p(\{y_i\}_i | \{x_i\}_i; \theta) = \sum_{i=1}^N -\log p(y_i | x_i; \theta)$, where each term is given by,

$$-\log p(y_i | x_i; \theta) = \log \left(\int e^{f_\theta(x_i, y)} dy \right) - f_\theta(x_i, y_i). \quad (2)$$

This direct and straightforward training approach thus requires the evaluation of the generally intractable $Z(x, \theta) = \int e^{f_\theta(x, y)} dy$. Many fundamental computer vision tasks, such as object detection, keypoint estimation, and pose estimation, however rely on regression problems with a low-dimensional target space \mathcal{Y} . In such cases, effective finite approximations of $Z(x, \theta)$ can be applied. In some tasks, such as image-coordinate regression, this is naturally performed by a grid approximation, utilizing the dense prediction obtained by fully-convolutional networks. In this work, we however investigate a more generally applicable technique, namely Monte Carlo approximations with importance sampling. This procedure, when employed for training the network, is detailed in Section 3.2.

At test time, given an input x^* , our model in (1) allows evaluating the conditional target density $p(y|x^*; \theta)$ for any target y by first approximating the constant $Z(x^*, \theta)$ and then predicting the scalar $f_\theta(x^*, y)$ using the DNN. This enables the computation of, for instance, the mean and variance of the target value y . In this work, we focus on finding the most likely prediction, $y^* = \arg \max_y p(y|x^*; \theta) =$

$\arg \max_y f_\theta(x^*, y)$, which does not require the evaluation of $Z(x, \theta)$ during inference. Thanks to the auto-differentiation capabilities of modern deep learning frameworks, we can apply gradient-based techniques to find the final prediction by simply maximizing the network output $f_\theta(x^*, y)$ w.r.t. y . We elaborate on this procedure for prediction in Section 3.3.

3.2. Training

Our model $p(y|x; \theta) = e^{f_\theta(x,y)}/Z(x, \theta)$ of the conditional target density is trained by directly minimizing the negative log-likelihood $\sum_{i=1}^N -\log p(y_i|x_i; \theta)$. To evaluate the integral in (2), we employ a Monte Carlo approximation with importance sampling. Specifically, each term $-\log p(y_i|x_i; \theta)$ is approximated by sampling values $\{y^{(k)}\}_{k=1}^M$ from a proposal distribution $q(y|y_i)$ that depends on the ground truth target value y_i ,

$$-\log p(y_i|x_i; \theta) \approx \log \left(\frac{1}{M} \sum_{k=1}^M \frac{e^{f_\theta(x_i, y^{(k)})}}{q(y^{(k)}|y_i)} \right) - f_\theta(x_i, y_i). \quad (3)$$

The final loss $J(\theta)$ is then obtained by averaging over all training samples $\{(x_i, y_i)\}_{i=1}^n$ in the current mini-batch,

$$J(\theta) = \frac{1}{n} \sum_{i=1}^n \log \left(\frac{1}{M} \sum_{m=1}^M \frac{e^{f_\theta(x_i, y^{(i,m)})}}{q(y^{(i,m)}|y_i)} \right) - f_\theta(x_i, y_i), \quad (4)$$

where $\{y^{(i,m)}\}_{m=1}^M$ are M samples drawn from $q(y|y_i)$. Qualitatively, minimizing $J(\theta)$ encourages the DNN to output large values $f_\theta(x_i, y_i)$ for the ground truth target y_i , while minimizing the predicted value $f_\theta(x_i, y)$ at all other targets y . In ambiguous or uncertain cases, the DNN can output small values everywhere or large values at multiple hypotheses, but at a cost of a higher loss.

As can be seen in (4), the DNN f_θ is applied both to the input-target pair (x_i, y_i) , and all input-sample pairs $\{(x_i, y^{(i,m)})\}_{m=1}^M$ during training. While this can seem inefficient, most applications in computer vision employ network architectures that first extract a deep feature representation for the input x_i . The DNN f_θ can thus be designed to combine this input feature with the target y at a late stage, as visualized in Figure 1. The input feature extraction process, which becomes the main computational bottleneck, therefore needs to be performed only once for each x_i . In practice, we found our training strategy to not add any significant overhead compared to the direct regression baselines, and the computational cost to be identical to that of the confidence-based methods.

Compared to confidence-based regression, a significant advantage of our approach is however that there is no need for generating task-dependent pseudo label confidences or choosing between different losses. The only design choice of our method is the proposal distribution $q(y|y_i)$. Note

Algorithm 1 Prediction via gradient-based refinement.

Input: $x^*, \hat{y}, T, \lambda, \eta$.

```

1:  $y \leftarrow \hat{y}$ .
2: for  $t = 1, \dots, T$  do
3:   PrevValue  $\leftarrow f_\theta(x^*, y)$ .
4:    $\tilde{y} \leftarrow y + \lambda \nabla_y f_\theta(x^*, y)$ .
5:   NewValue  $\leftarrow f_\theta(x^*, \tilde{y})$ .
6:   if NewValue > PrevValue then
7:      $y \leftarrow \tilde{y}$ .
8:   else
9:      $\lambda \leftarrow \lambda \cdot \eta$ .
10: Return  $y$ .

```

however that since the loss $J(\theta)$ in (4) explicitly adapts to $q(y|y_i)$, this choice has no effect on the overall behaviour of the loss, only on the quality of the sampled approximation. We found a mixture of a few equally weighted Gaussian components, all centered at the target label y_i , to consistently perform well in our experiments. Specifically we set,

$$q(y|y_i) = \frac{1}{L} \sum_{l=1}^L \mathcal{N}(y; y_i, \sigma_l^2), \quad (5)$$

where the variances $\{\sigma_l^2\}_{l=1}^L$ are hyperparameters selected based on a validation set for each experiment. Figure 2 illustrates that $p(y|x; \theta)$ can learn complex conditional target densities, containing both multi-modalities and asymmetry, directly from data using the described training procedure.

3.3. Prediction

Given an input x^* at test time, the trained DNN f_θ can be used to evaluate the full conditional target density $p(y|x^*; \theta) = e^{f_\theta(x^*, y)}/Z(x^*, \theta)$, by employing the aforementioned techniques to approximate the constant $Z(x^*, \theta)$. In many applications, the most likely prediction $y^* = \arg \max_y p(y|x^*; \theta)$ is however the single desired output. For our model, this is obtained by directly maximizing the DNN output, $y^* = \arg \max_y f_\theta(x^*, y)$, thus not requiring $Z(x^*, \theta)$ to be evaluated. By designing the DNN f_θ to be differentiable w.r.t. the target y , the gradient $\nabla_y f_\theta(x^*, y)$ can be efficiently evaluated using the auto-differentiation tools implemented in modern deep learning frameworks. We can therefore perform gradient ascent to find a local maximum of $f_\theta(x^*, y)$.

The gradient ascent refinement is performed either on a single initial estimate \hat{y} , or on a set of random initializations $\{\hat{y}_k\}_{k=1}^K$ to obtain a final accurate prediction y^* . As noted in Section 3.2, this prediction procedure can be made highly efficient in practice by extracting the deep feature representation for x^* only once. Back-propagation is then performed only through a few final layers of the DNN f_θ in order to evaluate the gradient $\nabla_y f_\theta(x^*, y)$. Moreover, the

Formulation Approach	Direct Faster-RCNN	Gaussian	Laplace	Confidence IoU-Net	Confidence IoU-Net*	Ours
AP (%)	37.2	36.7	37.1	38.3	38.2	39.1
AP ₅₀ (%)	59.2	58.7	59.1	58.3	58.4	58.5
AP ₇₅ (%)	40.3	39.6	40.2	41.4	41.4	41.8

Table 1: Results for the object detection task on the test-dev split of the COCO dataset [37]. Our proposed method significantly outperforms the baseline Faster-RCNN and the confidence-based IoU-Net.

gradient computation for a set of target candidates $\{\hat{y}_k\}_{k=1}^K$ can be parallelized on the GPU by simple batching, requiring no significant overhead. The prediction procedure is further detailed in Algorithm 1, where T denotes the number of gradient ascent iterations, λ is the step-length and η is a decay of the step-length.

4. Experiments

We perform comprehensive experiments on four different computer vision regression tasks: object detection, visual tracking, age estimation and head-pose estimation. Our proposed approach is compared both to baseline regression methods and to state-of-the-art models. Notably, our method significantly outperforms the confidence-based IoU-Net [27] method for bounding box regression in direct comparisons, both when applied for object detection on the COCO dataset [37], and for target object estimation in the recent ATOM [8] visual tracker. On the tasks of age and head-pose estimation, our approach is shown to consistently improve performance of a variety of baselines. All experiments are implemented in PyTorch [48].

4.1. Object detection

We first perform experiments for visual object detection, the problem of estimating a bounding box for each object in the image from a set of given classes. Specifically, we compare our regression method to other techniques for the task of bounding box regression, by integrating them into an existing object detection pipeline. To this end, we use the Faster-RCNN [53] framework, which serves as a popular baseline in the object detection field due to its strong state-of-the-art performance. It uses one network head for classification and the second for regressing the bounding box using the direct method. We also compare our approach to the confidence-based IoU-Net [27]. It extends Faster-RCNN with an additional branch that predicts the IoU overlap between a target bounding box y and the ground truth. The IoU prediction branch uses differentiable region pooling [27], allowing the initial bounding box predicted by the Faster-RCNN to be refined using gradient-based maximization of the predicted IoU confidence.

For our approach, we employ an identical architecture as used in IoU-Net for a fair comparison. Instead of training the network to output the IoU, we predict the expo-

nent $f_\theta(x, y)$ in (1), trained by minimizing the negative log-likelihood (NLL) in (4). We parametrize the bounding box as $y = (c_x/w_0, c_y/h_0, \log w, \log h) \in \mathbb{R}^4$, where (c_x, c_y) and (w, h) denote the center coordinate and size respectively. The reference size (w_0, h_0) is set to that of the ground truth during training and the initial box during inference. For the proposal distribution (5) we employ $L = 3$ isotropic Gaussians with standard deviation $\sigma_l = 0.05 \cdot 2^l$. In addition to the standard IoU-Net, we compare with a version (denoted IoU-Net*) employing the same proposal distribution and inference settings as in our approach. For both our method and IoU-Net*, we set the refinement step-length using grid search on a separate validation set. We also compare with a Gaussian and a Laplace probabilistic model for bounding box regression by modifying the Faster-RCNN regression head to predict both the mean and log-variance of the distribution, and adopting the NLL loss.

Our experiments are performed on the large-scale COCO benchmark [37]. As per the official guideline, we use the 2017 train split ($\approx 118\,000$ images) for training and the 2017 val split ($\approx 5\,000$ images) as the validation set for setting the hyperparameters. The results are reported on the 2017 test-dev split ($\approx 20\,000$ images), in terms of the standard COCO metrics AP (mean Average Precision AP_T over

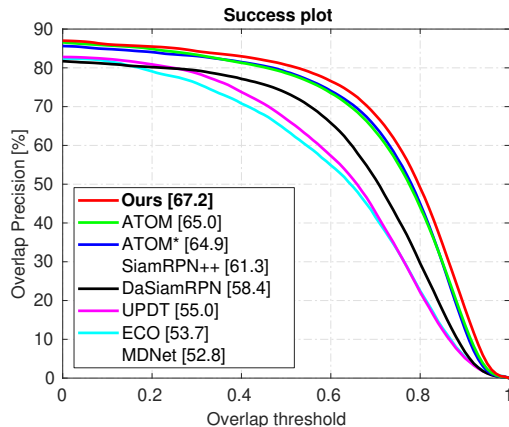


Figure 3: Success plot on the UAV123 [42] visual tracking dataset, showing the overlap precision OP_T as a function of the overlap threshold T . The proposed approach outperforms all previous methods, particularly for large overlap thresholds, indicating highly accurate predictions.

Dataset	Metric	ECO [9]	SiamFC [1]	MDNet [43]	UPDT [2]	DaSiamRPN [69]	SiamRPN++ [35]	ATOM [8]	ATOM*	Ours
TrackingNet [41]	Precision (%)	49.2	53.3	56.5	55.7	59.1	69.4	64.8	66.6	69.7
	Norm. Prec. (%)	61.8	66.6	70.5	70.2	73.3	80.0	77.1	78.4	80.1
	Success (%)	55.4	57.1	60.6	61.1	63.8	73.3	70.3	72.0	74.5
UAV123 [42]	OP _{0.50} (%)	64.0	-	-	66.8	73.6	75 [†]	78.9	79.0	80.8
	OP _{0.75} (%)	32.8	-	-	32.9	41.1	56 [†]	55.7	56.5	60.2
	AUC (%)	53.7	-	52.8	55.0	58.4	61.3	65.0	64.9	67.2

Table 2: Results for the visual tracking task on the two datasets TrackingNet [41] and UAV123 [42]. The symbol [†] indicate an approximate value (± 1), taken from the plot in the corresponding paper, due to the unavailability of the raw results. Our proposed method significantly outperforms the baseline ATOM and other state-of-the-art trackers.



Figure 4: Visualization of the conditional target density $p(y|x; \theta) \propto e^{f_\theta(x,y)}$ predicted by our network for the task of bounding box estimation in visual tracking. Since the target space $y \in \mathbb{R}^4$ is 4-dimensional, we visualize the density for different locations of the top-right corner as a heatmap, while the bottom-left is kept fixed at the tracker output (red box). Our network predicts flexible densities, expressing meaningful uncertainties in challenging cases.

10 IoU thresholds $T \in [0.5, 0.95]$, AP₅₀, and AP₇₅. We initialize all networks in our comparison with the pre-trained Faster-RCNN weights, using the ResNet50-FPN [36] backbone and re-train *only* the newly added layers for a fair comparison. Further details are provided in the supplementary material. The results are shown in Table 1. Our proposed method obtains the best results, outperforming both Faster-RCNN and IoU-Net by 1.9% and 0.8% in AP, respectively.

4.2. Visual tracking

Next, we evaluate our approach on the problem of generic visual object tracking. The task is to estimate the bounding box of a target object in every frame of a video. The target object is defined by a given box in the first video frame. We employ the recently introduced ATOM [8] tracker as our baseline. Given the first-frame annotation, ATOM trains a classifier to first roughly localize the target in a new frame. The target bounding box is then determined using an IoU-Net based module, which is also conditioned on the first-frame target appearance using a modulation-based architecture. We train our network to predict the conditional target density through $f_\theta(x, y)$ in (1), using a network architecture identical to the baseline ATOM tracker. In particular, we employ the same bounding box parameterization as for object detection (Section 4.1) and sample $M = 128$ boxes during training from a proposal distribution (5) generated by $L = 2$ Gaussians with standard deviations of 0.05 and 0.5. During tracking, we follow the same procedure as in ATOM, sampling 10 boxes in each frame

followed by gradient ascent to refine the estimate generated by the classification module.

We demonstrate results on two standard tracking benchmarks: TrackingNet [41] and UAV123 [42]. TrackingNet contains challenging videos sampled from YouTube, with a test set of 511 videos. The main metric is the Success, defined as the average IoU overlap with the ground truth. UAV123 contains 123 videos captured from a UAV, and includes small and fast-moving objects. We report the overlap precision metric (OP_T), defined as the percentage of frames having bounding box IoU overlap larger than a threshold T . The final AUC score is computed as the average OP over all thresholds $T \in [0, 1]$. Hyperparameters are set on the OTB [61] and NFS [15] datasets, containing 100 videos each. Due to the significant challenges imposed by the limited supervision and generic nature of the tracking problem, there are not any competitive baselines employing direct bounding box regression. Current state-of-the-art employ either confidence-based regression, as in ATOM, or anchor-based bounding box regression techniques [69, 35]. We therefore only compare with the ATOM baseline and include other recent state-of-the-art methods in the comparison. As in Section 4.1, we compare with a version of the IoU-Net based ATOM (denoted ATOM*) employing the same training and inference settings as our final approach. The results are shown in Table 2, and the success plot on UAV123 is shown in Figure 3. Our approach achieves a significant 2.5% and 2.2% absolute improvement over ATOM on the overall metric on TrackingNet and UAV123 respectively. Note that

+Refinement	Cao et al. [3]	Direct	Gaussian	Laplace	Softmax (CE, L^2)	Softmax (CE, L^2 , Var)
	5.47 \pm 0.01	4.81 \pm 0.02	4.79 \pm 0.06	4.85 \pm 0.04	4.78 \pm 0.05	4.81 \pm 0.03
✓	-	4.65 \pm 0.02	4.66 \pm 0.04	4.81 \pm 0.04	4.65 \pm 0.04	4.69 \pm 0.03

Table 3: Results for the age estimation experiments. Gradient-based refinement using our proposed method consistently improves MAE (lower is better) for the age predictions outputted by a number of baselines.

+Refinement	Yang et al. [64]	Direct	Gaussian	Laplace	Softmax (CE, L^2)	Softmax (CE, L^2 , Var)
	3.60	3.09 \pm 0.07	3.12 \pm 0.08	3.21 \pm 0.06	3.04 \pm 0.08	3.15 \pm 0.07
✓	-	3.07 \pm 0.07	3.11 \pm 0.07	3.19 \pm 0.06	3.01 \pm 0.07	3.11 \pm 0.06

Table 4: Results for the head-pose estimation experiments. Gradient-based refinement using our proposed method consistently improves the average MAE for Yaw, Pitch and Roll for the predicted pose outputted by our baselines.

the improvements are most prominent for high-accuracy boxes, indicated by the $OP_{0.75}$ score. Moreover, our approach outperforms the recent SiamRPN++ [35], which employs anchor-based bounding box regression [53, 52] and a much deeper backbone network (ResNet50) compared to ours (ResNet18). Figure 4 visualizes the conditional target density generated by our approach for tracking.

4.3. Age estimation

To demonstrate the general applicability of our proposed method, we also perform experiments on regression tasks not involving bounding boxes. In age estimation, we are given a cropped image $x \in \mathbb{R}^{h \times w \times 3}$ of a person’s face, and the task is to predict his/her age $y \in \mathbb{R}_+$. We utilize the UTKFace [67] dataset, specifically the subset of 16 434 images used by Cao et al. [3]. In this subset, ground truth age labels $y_i \in [21, 60]$. We also utilize the dataset split employed in [3], with 3 287 test images and 11 503 images for training. Additionally, we use 1 644 of the training images for validation. Methods are evaluated in terms of the Mean Absolute Error (MAE). The DNN architecture $f_\theta(x, y)$ of our model first extracts ResNet50 [21] features $g_x \in \mathbb{R}^{2048}$ from the input image x . The age y is processed by four fully-connected layers, generating $g_y \in \mathbb{R}^{128}$. The two feature vectors are then concatenated and processed by two fully-connected layers, outputting $f_\theta(x, y) \in \mathbb{R}$. We apply our proposed method to refine the age predicted by baseline models, using the gradient ascent maximization of $f_\theta(x, y)$ detailed in Section 3.3. All baseline DNN models employ a similar architecture, including an identical ResNet50 for feature extraction and the same number of fully-connected layers to output either the age $y \in \mathbb{R}$ (*Direct*), mean and variance parameters for Gaussian and Laplace distributions, or to output logits for C discretized classes (*Softmax*). The results are found in Table 3. We observe that age refinement provided by our method consistently improves the accuracy of the predictions generated by the baseline methods. The supplementary material contains a more detailed description of the experiments.

4.4. Head-pose estimation

Lastly, we evaluate our method on the task of head-pose estimation. In this case, we are given an image $x \in \mathbb{R}^{h \times w \times 3}$ of a person, and are tasked with predicting the orientation $y \in \mathbb{R}^3$ of his/her head, where y is the Yaw, Pitch and Roll angles. We utilize the BIWI [13] dataset, specifically the processed dataset provided by Yang et al. [64], in which the images have been cropped to faces detected using MTCNN [66]. We also employ protocol 2 as defined in [64], with 10 613 images for training and 5 065 images for testing. Additionally, we use 1 010 training images for validation. The methods are evaluated in terms of the average MAE for Yaw, Pitch and Roll. The network architecture of the DNN f_θ defining our model takes the image $x \in \mathbb{R}^{h \times w \times 3}$ and orientation $y \in \mathbb{R}^3$ as inputs, but is otherwise identical to the age estimation case (Section 4.3). Our model is again evaluated by applying the gradient-based refinement to the predicted orientation $y \in \mathbb{R}^3$ outputted by a number of baseline models. We use the same baselines as for age estimation, and apart from minor changes required to increase the output dimension from 1 to 3, identical network architectures are also used. The results are found in Table 4, and also in this case we observe that refinement using our proposed method consistently improves upon the baselines. Further details are provided in the supplementary material.

5. Conclusion

We proposed a general and conceptually simple regression method with a clear probabilistic interpretation. It models the conditional target density $p(y|x)$ by predicting the un-normalized density through a DNN $f_\theta(x, y)$, taking the input-target pair (x, y) as input. This energy-based model of $p(y|x)$ is trained by directly minimizing the associated negative log-likelihood, employing a Monte Carlo approximation of the partition function. At test time, targets are predicted by maximizing the DNN output $f_\theta(x, y)$ w.r.t. y via gradient-based refinement. Experiments performed on four diverse computer vision applications demonstrate

the high accuracy and wide applicability of our method. Future directions include exploring better architectural designs, studying other regression applications, and investigating our proposed method’s potential for aleatoric uncertainty estimation.

Acknowledgments

This research was financially supported by the Swedish Foundation for Strategic Research (SSF) via the project *ASSEMBLE* (contract number: RIT15-0012) and by the project *Learning flexible models for nonlinear dynamics* (contract number: 2017-03807), funded by the Swedish Research Council.

References

- [1] Luca Bertinetto, Jack Valmadre, João F Henriques, Andrea Vedaldi, and Philip HS Torr. Fully-convolutional siamese networks for object tracking. In *ECCV workshop*, 2016. 7
- [2] Goutam Bhat, Joakim Johnander, Martin Danelljan, Fahad Shahbaz Khan, and Michael Felsberg. Unveiling the power of deep tracking. In *ECCV*, 2018. 7
- [3] Wenzhi Cao, Vahid Mirjalili, and Sebastian Raschka. Rank-consistent ordinal regression for neural networks. *arXiv preprint arXiv:1901.07884*, 2019. 1, 4, 8, 15
- [4] Zhe Cao, Tomas Simon, Shih-En Wei, and Yaser Sheikh. Realtime multi-person 2d pose estimation using part affinity fields. In *Proceedings of the IEEE Conference on Computer Vision and Pattern Recognition (CVPR)*, pages 7291–7299, 2017. 1, 2
- [5] Chen-Rui Chou, Brandon Frederick, Gig Mageras, Sha Chang, and Stephen Pizer. 2D/3D image registration using regression learning. *Computer Vision and Image Understanding*, 117(9):1095–1106, 2013. 1
- [6] Kurtland Chua, Roberto Calandra, Rowan McAllister, and Sergey Levine. Deep reinforcement learning in a handful of trials using probabilistic dynamics models. In *Advances in Neural Information Processing Systems (NeurIPS)*, pages 4759–4770, 2018. 2, 3
- [7] Martin Danelljan and Goutam Bhat. PyTracking: Visual tracking library based on PyTorch. <https://github.com/visionml/pytracking>, 2019. Accessed: 12/08/2019. 13
- [8] Martin Danelljan, Goutam Bhat, Fahad Shahbaz Khan, and Michael Felsberg. ATOM: Accurate tracking by overlap maximization. In *Proceedings of the IEEE Conference on Computer Vision and Pattern Recognition (CVPR)*, pages 4660–4669, 2019. 1, 2, 3, 6, 7, 13
- [9] Martin Danelljan, Goutam Bhat, Fahad Shahbaz Khan, and Michael Felsberg. ECO: efficient convolution operators for tracking. In *CVPR*, 2017. 7
- [10] Raul Diaz and Amit Marathe. Soft labels for ordinal regression. In *Proceedings of the IEEE Conference on Computer Vision and Pattern Recognition (CVPR)*, 2019. 4
- [11] Yilun Du and Igor Mordatch. Implicit generation and modeling with energy based models. In *Advances in Neural Information Processing Systems (NeurIPS)*, 2019. 4
- [12] Heng Fan, Liting Lin, Fan Yang, Peng Chu, Ge Deng, Sijia Yu, Hexin Bai, Yong Xu, Chunyuan Liao, and Haibin Ling. Lasot: A high-quality benchmark for large-scale single object tracking. In *CVPR*, 2019. 14
- [13] Gabriele Fanelli, Matthias Dantone, Juergen Gall, Andrea Fossati, and Luc Van Gool. Random forests for real time 3d face analysis. *International Journal of Computer Vision (IJCV)*, 101(3):437–458, 2013. 8
- [14] Di Feng, Lars Rosenbaum, Fabian Timm, and Klaus Dietmayer. Leveraging heteroscedastic aleatoric uncertainties for robust real-time lidar 3D object detection. In *2019 IEEE Intelligent Vehicles Symposium (IV)*, pages 1280–1287. IEEE, 2019. 3
- [15] Hamed Kiani Galoogahi, Ashton Fagg, Chen Huang, Deva Ramanan, and Simon Lucey. Need for speed: A benchmark for higher frame rate object tracking. In *ICCV*, 2017. 7
- [16] Ruiqi Gao, Yang Lu, Junpei Zhou, Song-Chun Zhu, and Ying Nian Wu. Learning generative convnets via multi-grid modeling and sampling. In *Proceedings of the IEEE Conference on Computer Vision and Pattern Recognition (CVPR)*, pages 9155–9164, 2018. 4
- [17] Jochen Gast and Stefan Roth. Lightweight probabilistic deep networks. In *Proceedings of the IEEE Conference on Computer Vision and Pattern Recognition (CVPR)*, pages 3369–3378, 2018. 2, 3, 16
- [18] Ross B. Girshick. Fast r-cnn. *2015 IEEE International Conference on Computer Vision (ICCV)*, pages 1440–1448, 2015. 12
- [19] Jinwei Gu, Xiaodong Yang, Shalini De Mello, and Jan Kautz. Dynamic facial analysis: From bayesian filtering to recurrent neural network. In *Proceedings of the IEEE Conference on Computer Vision and Pattern Recognition (CVPR)*, pages 1548–1557, 2017. 17
- [20] Kaiming He, Georgia Gkioxari, Piotr Dollár, and Ross B. Girshick. Mask r-cnn. *2017 IEEE International Conference on Computer Vision (ICCV)*, pages 2980–2988, 2017. 12
- [21] Kaiming He, Xiangyu Zhang, Shaoqing Ren, and Jian Sun. Deep residual learning for image recognition. In *Proceedings of the IEEE Conference on Computer Vision and Pattern Recognition (CVPR)*, pages 770–778, 2016. 8
- [22] Yihui He, Chenchen Zhu, Jianren Wang, Marios Savvides, and Xiangyu Zhang. Bounding box regression with uncertainty for accurate object detection. In *Proceedings of the IEEE Conference on Computer Vision and Pattern Recognition (CVPR)*, pages 2888–2897, 2019. 3
- [23] Geoffrey Hinton, Simon Osindero, Max Welling, and Yee-Whye Teh. Unsupervised discovery of nonlinear structure using contrastive backpropagation. *Cognitive science*, 30(4):725–731, 2006. 4
- [24] Lianghua Huang, Xin Zhao, and Kaiqi Huang. GOT-10k: A large high-diversity benchmark for generic object tracking in the wild. *arXiv preprint arXiv:1810.11981*, 2018. 14
- [25] Peter J Huber. Robust estimation of a location parameter. *The Annals of Mathematical Statistics*, pages 73–101, 1964. 3, 12

- [26] Eddy Ilg, Ozgun Cicek, Silvio Galesso, Aaron Klein, Osama Makansi, Frank Hutter, and Thomas Bro. Uncertainty estimates and multi-hypotheses networks for optical flow. In *Proceedings of the European Conference on Computer Vision (ECCV)*, pages 652–667, 2018. [2](#), [3](#)
- [27] Borui Jiang, Ruixuan Luo, Jiayuan Mao, Tete Xiao, and Yuning Jiang. Acquisition of localization confidence for accurate object detection. In *Proceedings of the European Conference on Computer Vision (ECCV)*, pages 784–799, 2018. [1](#), [2](#), [3](#), [6](#), [12](#), [13](#)
- [28] Alex Kendall and Yarin Gal. What uncertainties do we need in Bayesian deep learning for computer vision? In *Advances in Neural Information Processing Systems (NeurIPS)*, pages 5574–5584, 2017. [2](#), [3](#)
- [29] Diederik P Kingma and Jimmy Ba. Adam: A method for stochastic optimization. *arXiv preprint arXiv:1412.6980*, 2014. [12](#)
- [30] Balaji Lakshminarayanan, Alexander Pritzel, and Charles Blundell. Simple and scalable predictive uncertainty estimation using deep ensembles. In *Advances in Neural Information Processing Systems (NeurIPS)*, pages 6402–6413, 2017. [2](#), [3](#)
- [31] Stéphane Lathuilière, Pablo Mesejo, Xavier Alameda-Pineda, and Radu Horaud. A comprehensive analysis of deep regression. *IEEE Transactions on Pattern Analysis and Machine Intelligence (TPAMI)*, 2019. [1](#), [3](#)
- [32] Hei Law and Jia Deng. Cornernet: Detecting objects as paired keypoints. In *Proceedings of the European Conference on Computer Vision (ECCV)*, pages 734–750, 2018. [1](#), [2](#), [3](#)
- [33] Dieterich Lawson, George Tucker, Bo Dai, and Rajesh Ranganath. Energy-inspired models: Learning with sampler-induced distributions. In *Advances in Neural Information Processing Systems (NeurIPS)*, 2019. [4](#)
- [34] Yann LeCun, Sumit Chopra, Raia Hadsell, M Ranzato, and F Huang. A tutorial on energy-based learning. *Predicting structured data*, 1(0), 2006. [2](#), [4](#)
- [35] Bo Li, Wei Wu, Qiang Wang, Fangyi Zhang, Junliang Xing, and Junjie Yan. Siamrpn++: Evolution of siamese visual tracking with very deep networks. In *CVPR*, 2019. [1](#), [7](#), [8](#)
- [36] Tsung-Yi Lin, Piotr Dollár, Ross Girshick, Kaiming He, Bharath Hariharan, and Serge Belongie. Feature pyramid networks for object detection. In *Proceedings of the IEEE Conference on Computer Vision and Pattern Recognition (CVPR)*, pages 2117–2125, 2017. [2](#), [7](#), [12](#)
- [37] Tsung-Yi Lin, Michael Maire, Serge Belongie, James Hays, Pietro Perona, Deva Ramanan, Piotr Dollár, and C Lawrence Zitnick. Microsoft coco: Common objects in context. In *Proceedings of the European Conference on Computer Vision (ECCV)*, pages 740–755, 2014. [2](#), [6](#), [12](#)
- [38] Wei Liu, Dragomir Anguelov, Dumitru Erhan, Christian Szegedy, Scott Reed, Cheng-Yang Fu, and Alexander C Berg. SSD: Single shot multibox detector. In *Proceedings of the European Conference on Computer Vision (ECCV)*, pages 21–37. Springer, 2016. [4](#)
- [39] Francisco Massa and Ross Girshick. maskrcnn-benchmark: Fast, modular reference implementation of Instance Segmentation and Object Detection algorithms in PyTorch. <https://github.com/facebookresearch/maskrcnn-benchmark>, 2018. Accessed: 04/09/2019. [12](#), [13](#)
- [40] Andriy Mnih and Geoffrey Hinton. Learning nonlinear constraints with contrastive backpropagation. In *Proceedings of the IEEE International Joint Conference on Neural Networks*, volume 2, pages 1302–1307. IEEE, 2005. [4](#)
- [41] Matthias Müller, Adel Bibi, Silvio Giancola, Salman Al-Subaihi, and Bernard Ghanem. Trackingnet: A large-scale dataset and benchmark for object tracking in the wild. In *ECCV*, 2018. [2](#), [7](#), [14](#)
- [42] Matthias Müller, Neil Smith, and Bernard Ghanem. A benchmark and simulator for uav tracking. In *ECCV*, 2016. [2](#), [6](#), [7](#)
- [43] Hyeonseob Nam and Bohyung Han. Learning multi-domain convolutional neural networks for visual tracking. In *CVPR*, 2016. [1](#), [7](#)
- [44] Marc Niethammer, Yang Huang, and François-Xavier Vialard. Geodesic regression for image time-series. In *International conference on medical image computing and computer-assisted intervention*, pages 655–662. Springer, 2011. [1](#)
- [45] Erik Nijkamp, Mitch Hill, Tian Han, Song-Chun Zhu, and Ying Nian Wu. On the anatomy of mcmc-based maximum likelihood learning of energy-based models. *arXiv preprint arXiv:1903.12370*, 2019. [4](#)
- [46] Zhenxing Niu, Mo Zhou, Le Wang, Xinbo Gao, and Gang Hua. Ordinal regression with multiple output cnn for age estimation. In *Proceedings of the IEEE Conference on Computer Vision and Pattern Recognition (CVPR)*, pages 4920–4928, 2016. [15](#)
- [47] Hongyu Pan, Hu Han, Shiguang Shan, and Xilin Chen. Mean-variance loss for deep age estimation from a face. In *Proceedings of the IEEE Conference on Computer Vision and Pattern Recognition (CVPR)*, pages 5285–5294, 2018. [1](#), [3](#), [4](#), [15](#), [16](#)
- [48] Adam Paszke, Sam Gross, Soumith Chintala, Gregory Chanan, Edward Yang, Zachary DeVito, Zeming Lin, Alban Desmaison, Luca Antiga, and Adam Lerer. Automatic differentiation in PyTorch. In *NeurIPS - Autodiff Workshop*, 2017. [6](#)
- [49] Leonid Pishchulin, Eldar Insafutdinov, Siyu Tang, Bjoern Andres, Mykhaylo Andriluka, Peter V. Gehler, and Bernt Schiele. Deepcut: Joint subset partition and labeling for multi person pose estimation. In *2016 IEEE Conference on Computer Vision and Pattern Recognition, CVPR 2016, Las Vegas, NV, USA, June 27-30, 2016*, pages 4929–4937, 2016. [3](#)
- [50] Charles R Qi, Wei Liu, Chenxia Wu, Hao Su, and Leonidas J Guibas. Frustum PointNets for 3D object detection from RGB-D data. In *Proceedings of the IEEE Conference on Computer Vision and Pattern Recognition (CVPR)*, pages 918–927, 2018. [4](#)
- [51] Joseph Redmon, Santosh Divvala, Ross Girshick, and Ali Farhadi. You only look once: Unified, real-time object detection. In *Proceedings of the IEEE Conference on Computer Vision and Pattern Recognition (CVPR)*, pages 779–788, 2016. [4](#)

- [52] Joseph Redmon and Ali Farhadi. Yolo9000: Better, faster, stronger. *2017 IEEE Conference on Computer Vision and Pattern Recognition (CVPR)*, pages 6517–6525, 2016. [8](#)
- [53] Shaoqing Ren, Kaiming He, Ross B. Girshick, and Jian Sun. Faster r-cnn: Towards real-time object detection with region proposal networks. *IEEE Transactions on Pattern Analysis and Machine Intelligence*, 39:1137–1149, 2015. [1](#), [3](#), [6](#), [8](#), [12](#)
- [54] Rasmus Rothe, Radu Timofte, and Luc Van Gool. Deep expectation of real and apparent age from a single image without facial landmarks. *International Journal of Computer Vision*, 126(2-4):144–157, 2016. [1](#), [3](#), [4](#)
- [55] Nataniel Ruiz, Eunji Chong, and James M Rehg. Fine-grained head pose estimation without keypoints. In *Proceedings of the IEEE Conference on Computer Vision and Pattern Recognition Workshops*, pages 2074–2083, 2018. [4](#)
- [56] Shaoshuai Shi, Xiaogang Wang, and Hongsheng Li. Pointcnn: 3d object proposal generation and detection from point cloud. In *Proceedings of the IEEE Conference on Computer Vision and Pattern Recognition (CVPR)*, pages 770–779, 2019. [4](#)
- [57] Tomas Simon, Hanbyul Joo, Iain A. Matthews, and Yaser Sheikh. Hand keypoint detection in single images using multiview bootstrapping. In *2017 IEEE Conference on Computer Vision and Pattern Recognition, CVPR 2017, Honolulu, HI, USA, July 21-26, 2017*, pages 4645–4653, 2017. [3](#)
- [58] Ke Sun, Bin Xiao, Dong Liu, and Jingdong Wang. Deep high-resolution representation learning for human pose estimation. In *CVPR*, 2019. [1](#), [2](#), [3](#)
- [59] Ioannis Tsochantaridis, Thorsten Joachims, Thomas Hofmann, and Yasemin Altun. Large margin methods for structured and interdependent output variables. *J. Mach. Learn. Res.*, 6:1453–1484, 2005. [3](#)
- [60] Shih-En Wei, Varun Ramakrishna, Takeo Kanade, and Yaser Sheikh. Convolutional pose machines. In *2016 IEEE Conference on Computer Vision and Pattern Recognition, CVPR 2016, Las Vegas, NV, USA, June 27-30, 2016*, pages 4724–4732, 2016. [2](#), [3](#)
- [61] Yi Wu, Jongwoo Lim, and Ming-Hsuan Yang. Object tracking benchmark. *TPAMI*, 37(9):1834–1848, 2015. [7](#)
- [62] Bin Xiao, Haiping Wu, and Yichen Wei. Simple baselines for human pose estimation and tracking. In *Proceedings of the European Conference on Computer Vision (ECCV)*, pages 466–481, 2018. [1](#), [2](#), [3](#)
- [63] Jianwen Xie, Yang Lu, Song-Chun Zhu, and Yingnian Wu. A theory of generative convnet. In *International Conference on Machine Learning (ICML)*, pages 2635–2644, 2016. [4](#)
- [64] Tsun-Yi Yang, Yi-Ting Chen, Yen-Yu Lin, and Yung-Yu Chuang. FSA-Net: Learning fine-grained structure aggregation for head pose estimation from a single image. In *Proceedings of the IEEE Conference on Computer Vision and Pattern Recognition (CVPR)*, pages 1087–1096, 2019. [1](#), [4](#), [8](#), [17](#)
- [65] Tsun-Yi Yang, Yi-Hsuan Huang, Yen-Yu Lin, Pi-Cheng Hsiu, and Yung-Yu Chuang. SSR-Net: A compact soft stage-wise regression network for age estimation. In *Proceedings of the International Joint Conference on Artificial Intelligence (IJCAI)*, 2018. [4](#), [17](#)
- [66] Kaipeng Zhang, Zhanpeng Zhang, Zhifeng Li, and Yu Qiao. Joint face detection and alignment using multitask cascaded convolutional networks. *IEEE Signal Processing Letters*, 23(10):1499–1503, 2016. [8](#)
- [67] Zhifei Zhang, Yang Song, and Hairong Qi. Age progression/regression by conditional adversarial autoencoder. In *Proceedings of the IEEE Conference on Computer Vision and Pattern Recognition (CVPR)*, pages 5810–5818, 2017. [8](#)
- [68] Xingyi Zhou, Jiacheng Zhuo, and Philipp Krahenbuhl. Bottom-up object detection by grouping extreme and center points. In *Proceedings of the IEEE Conference on Computer Vision and Pattern Recognition (CVPR)*, pages 850–859, 2019. [1](#), [2](#), [3](#)
- [69] Zheng Zhu, Qiang Wang, Li Bo, Wei Wu, Junjie Yan, and Weiming Hu. Distractor-aware siamese networks for visual object tracking. In *ECCV*, 2018. [1](#), [7](#)

Supplementary Material

In this supplementary material we provide additional details and results. It consists of Appendix A - Appendix E. Appendix A contains details on the illustrative 1D regression problem in Figure 2 in the main paper. Further details on the employed training and inference procedures are provided in Appendix B for the object detection experiments, and in Appendix C for the visual tracking experiments. Lastly, Appendix D and Appendix E contain details and full results for the experiments on age estimation and head-pose estimation, respectively. Note that equations, tables, figures and algorithms in this supplementary document are numbered with the prefix "S". Numbers without this prefix refer to the main paper.

Appendix A. Illustrative example

The ground truth conditional target density $p(y|x)$ in Figure 2 is defined by a mixture of two Gaussian components (with weights 0.2 and 0.8) for $x < 0$, and a log-normal distribution (with $\mu = 0.0$, $\sigma = 0.25$) for $x \geq 0$. The training data $\{(x_i, y_i)\}_{i=1}^{2000}$ was generated by uniform random sampling of x , $x_i \sim U(-3, 3)$. Both models were trained for 75 epochs with a batch size of 32 using the ADAM [29] optimizer.

The Gaussian model is defined using a DNN $f_\theta(x)$ according to,

$$\begin{aligned} p(y|x; \theta) &= \mathcal{N}(y; \mu_\theta(x), \sigma_\theta^2(x)), \\ f_\theta(x) &= [\mu_\theta(x) \quad \log \sigma_\theta^2(x)]^\top \in \mathbb{R}^2. \end{aligned} \quad (\text{S1})$$

It is trained by minimizing the negative log-likelihood, corresponding to the loss,

$$J(\theta) = \frac{1}{n} \sum_{i=1}^n \frac{(y_i - \mu_\theta(x_i))^2}{\sigma_\theta^2(x_i)} + \log \sigma_\theta^2(x_i). \quad (\text{S2})$$

The DNN f_θ is a simple feed-forward neural network, containing two shared fully-connected layers (dimensions: $1 \rightarrow 10$, $10 \rightarrow 10$) and two identical heads for μ and $\log \sigma^2$ of three fully-connected layers ($10 \rightarrow 10$, $10 \rightarrow 10$, $10 \rightarrow 1$).

Our proposed model $p(y|x; \theta) = e^{f_\theta(x,y)} / Z(x, \theta)$ (Eq. 1 in the paper) is defined using a feed-forward neural network $f_\theta(x, y)$ containing two fully-connected layers ($1 \rightarrow 10$, $10 \rightarrow 10$) for both x and y , and three fully-connected layers ($20 \rightarrow 10$, $10 \rightarrow 10$, $10 \rightarrow 1$) processing the concatenated (x, y) feature vector. It is trained using $M = 1024$ samples from a proposal distribution $q(y|y_i)$ (Eq. 5 in the paper) with $L = 2$ and variances $\sigma_1^2 = 0.1^2$, $\sigma_2^2 = 0.8^2$.

Appendix B. Object detection

Here, we provide further details about the network architectures, training procedure, and hyperparameters used

for our experiments on object detection (Section 4.1 in the paper).

B.1. Network architecture

We use the Faster-RCNN [53] detector with ResNet50-FPN [36] as our baseline. As visualized in Figure S1a, Faster-RCNN generates object proposals using a region proposal network (RPN). The features from the proposal regions are then pooled to a fixed-sized feature map using the RoiPool layer [18]. The pooled features are then passed through a feature extractor (denoted Feat-Box) consisting of two fully-connected (FC) layers. The output feature vector is then passed through two parallel FC layers, one which predicts the class label (denoted FC-Cls), and another which regresses the offsets between the proposal and the ground truth box (denoted FC-BB). We use the PyTorch implementation for Faster-RCNN from [39]. Note that we use the RoiAlign [20] layer instead of RoiPool in our experiments as it has been shown to achieve better performance [20].

For the Gaussian and Laplace probabilistic models (Gaussian and Laplace in Table 1 in the paper), we replace the FC-BBReg layer in Faster-RCNN with two parallel FC layers, denoted FC-BBMean and FC-BBVar, which predict the mean and the log-variance of the distribution modeling the offset between the proposal and the ground truth box for each coordinate. This architecture is shown in Figure S1b.

For our confidence-based IoU-Net [27] models (IoU-Net and IoU-Net* in Table 1), we use the same network architecture as employed in the original paper, shown in Figure S1c. That is, we add an additional branch to predict the IoU overlap between the proposal box and the ground truth. This branch uses the PrRoiPool [27] layer to pool the features from the proposal regions. The pooled features are passed through a feature extractor (denoted Feat-Conf) consisting of two FC layers. The output feature vector is passed through another FC layer, FC-Conf, which predicts the IoU. We use an identical architecture for our approach, but train it to output $f_\theta(x, y)$ in $p(y|x; \theta) = e^{f_\theta(x,y)} / Z(x, \theta)$ instead. Illustrations of all architectures are found in Figure S1.

B.2. Training

We use the pre-trained weights for Faster-RCNN from [39]. Note that the bounding box regression in Faster-RCNN is trained using a direct method, with an Huber loss [25]. We trained the other networks in Table 1 in the paper (Gaussian, Laplace, IoU-Net, IoU-Net* and Ours) on the MS-COCO [37] training split (2017 train) using stochastic gradient descent (SGD) with a batch size of 16 for 60k iterations. The base learning rate lr_{base} is reduced by a factor of 10 after 40k and 50k iterations, for all the networks. We also warm up the training by linearly increasing the learning rate from $\frac{1}{3}lr_{\text{base}}$ to lr_{base} during the first 500 iterations. We use a weight decay of 0.0001 and a momen-

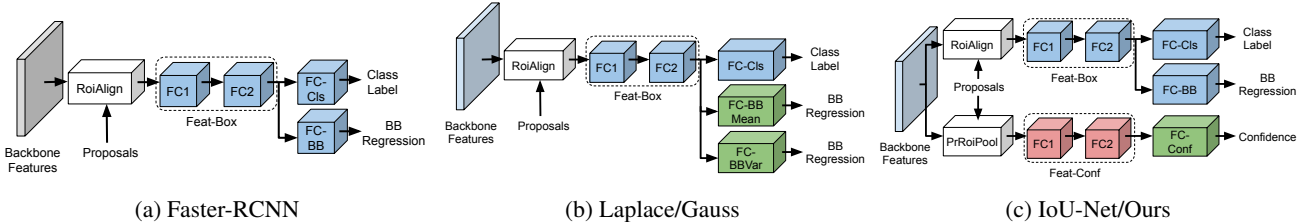


Figure S1: Network architectures for the different detection networks used in our experiments (Section 4.1 in the paper). The backbone feature extractor (ResNet50-FPN), and the region proposal network (RPN) is not shown for clarity. We do not train the blocks in blue color, using the pre-trained Faster-RCNN weights from [39] instead. The blocks in red are initialized with the pre-trained Faster-RCNN weights and fine-tuned. The blocks in green on the other hand are trained from scratch.

tum of 0.9. For all the networks, we only trained the newly added layers, while keeping the backbone and the region proposal network fixed.

For the Gaussian and Laplace models, we only train the final predictors (FC-BBMean and FC-BBVar), while keeping the class predictor (FC-Cls) and the box feature extractor (Feat-Box) fixed. We also tried fine-tuning the FC-Cls and Feat-Box weights, with different learning rate settings, but obtained worse performance on the validation set. The weights for both FC-BBMean and FC-BBVar were initialized with zero mean Gaussian with standard deviation of 0.001. Both Gaussian and Laplace models were trained with a base learning rate $lr_{\text{base}} = 0.005$ by minimizing the negative log-likelihood.

For the IoU-Net, IoU-Net* and our proposed model, we only trained the newly added confidence branch. We found it beneficial to initialize the feature extractor block (Feat-Conf) with the corresponding weights from Faster-RCNN, i.e. the Feat-Box block. The weights for the predictor FC-Conf were initialized with zero mean Gaussian with standard deviation of 0.001. As in the original paper [27], we used a base learning rate $lr_{\text{base}} = 0.01$ for the IoU-Net and IoU-Net* networks. For our proposed model, we used $lr_{\text{base}} = 0.001$ due to the different scaling of the loss. Note that we did not perform any parameter tuning for setting the learning rates. We generate 128 proposals for each ground truth box during training. For the IoU-Net, we use the proposal generation strategy mentioned in the original paper [27]. That is, for each ground truth box, we generate a large set of candidate boxes which have an IoU overlap of at least 0.5 with the ground truth, and uniformly sample 128 proposals from this candidate set w.r.t. the IoU. For IoU-Net* and our model, we sample boxes from a proposal distribution (Eq. 5 in the paper) generated by $L = 3$ Gaussians with standard deviations of 0.05, 0.1, and 0.2. The IoU-Net and IoU-Net* are trained by minimizing the Huber loss between the predicted IoU and the ground truth, while our model is trained by minimizing the negative log likelihood of the training data (Eq. 4 in the paper).

B.3. Inference

The inference in both Gaussian and Laplace models is identical to the one employed by Faster-RCNN. Thus, we do not utilize the predicted variances for inference. For IoU-Net and IoU-Net*, we perform IoU-Guided NMS as described in [27], followed by gradient-based refinement (Algorithm 1 in the paper). For our proposed approach we adopt the same NMS technique, but guide it with the values $f_{\theta}(x, y)$ predicted by our network instead. We use a step-length $\lambda = 0.5$ and step-length decay $\eta = 0.1$ for IoU-Net. For IoU-Net* and our approach we perform the gradient-based refinement in the relative bounding box parametrization $y = (c_x/w_0, c_y/h_0, \log w, \log h)$ (see Section 4.1 in the paper). Here, we employ different step-lengths for position and size. For IoU-Net*, we use $\lambda = 0.002$ and $\lambda = 0.008$ respectively, with a decay of $\eta = 0.2$. For our proposed approach, we use $\lambda = 0.0001$ and $\lambda = 0.0004$ with $\eta = 0.5$. For all methods, these hyperparameters (λ and η) were set using a grid search on the MS-COCO validation split (2017 val). We used $T = 10$ refinement iterations for each of the three models.

Appendix C. Visual tracking

Here, we provide further details about the training procedure and hyperparameters used for our experiments on visual object tracking (Section 4.2 in the paper).

C.1. Training

We adopt the ATOM [8] tracker as our baseline, and use the PyTorch implementation and pre-trained weights from [7]. ATOM trains an IoU-Net based module to predict the IoU overlap between a candidate box and the ground truth, conditioned on the first-frame target appearance. The IoU predictor is trained by generating 16 candidates for each ground truth box. The candidates are generated by adding a Gaussian noise for each ground truth box coordinate, while ensuring a minimum IoU overlap of 0.1 between the candidate box and the ground truth. The network is

trained by minimizing the squared error (L^2 loss) between the predicted and ground truth IoU.

Our proposed model is instead trained by sampling 128 candidate boxes from a proposal distribution (Eq. 5 in the paper) generated by $L = 2$ Gaussians with standard deviations of 0.05 and 0.5, and minimizing the negative log likelihood of the training data. We use the training splits of TrackingNet [41], LaSOT [12], GOT10k [24], and MS-COCO datasets for our training. Our network is trained for 50 epochs, using the ADAM optimizer with a base learning rate of 0.001 which is reduced by a factor of 5 after every 15 epochs. The rest of the training parameters are exactly the same as in ATOM. The ATOM* model is trained by using the exact same proposal distribution, datasets and settings. It only differs by the loss, which is the same squared error between the predicted and ground truth IoU as in the original ATOM.

C.2. Inference

During tracking, the ATOM tracker first applies the classification head network, which is trained online, to coarsely localize the target object. 10 random boxes are then sampled around this prediction, to be refined by the IoU prediction network. We only alter the final bounding box refinement step of the 10 given random initial boxes, and preserve all other settings as in the original ATOM tracker. The original version performs $T = 5$ gradient ascent iterations with a step length of $\lambda = 1.0$. For our proposed model and the ATOM* version, we use $T = 10$ iterations, employing the bounding box parameterization described in Section 4.1. For our approach we set the step length to $\lambda = 2 \cdot 10^{-4}$ for position and $\lambda = 10^{-3}$ for size dimensions. For ATOM* we use $\lambda = 10^{-2}$ for position and $\lambda = 5 \cdot 10^{-2}$ for size dimensions. These parameters were set on the separate validation set. For simplicity, we adopt the vanilla gradient ascent strategy employed in ATOM for the two other methods as well. That is, we have no decay ($\eta = 1$) and do not perform checks whether the confidence score is increasing in each iteration.

Appendix D. Age estimation

In this appendix, further details on the age estimation experiments (Section 4.3 in the paper) are provided.

D.1. Network architecture

The DNN architecture $f_\theta(x, y)$ of our proposed model first extracts ResNet50 features $g_x \in \mathbb{R}^{2048}$ from the input image x . The age y is processed by four fully-connected layers (dimensions: $1 \rightarrow 16, 16 \rightarrow 32, 32 \rightarrow 64, 64 \rightarrow 128$), generating $g_y \in \mathbb{R}^{128}$. The two feature vectors g_x, g_y are then concatenated to form $g_{x,y} \in \mathbb{R}^{2048+128}$, which is processed by two fully-connected layers ($2048 + 128 \rightarrow 2048, 2048 \rightarrow 1$), outputting $f_\theta(x, y) \in \mathbb{R}$.

D.2. Training

Our model is trained using $M = 1024$ samples from a proposal distribution $q(y|y_i)$ (Eq. 5 in the paper) with $L = 2$ and variances $\sigma_1^2 = 0.1^2, \sigma_2^2 = 20^2$. It is trained for 75 epochs with a batch size of 32, using the ADAM optimizer with weight decay of 0.001. The images x are of size 200×200 . For data augmentation, we use random flipping along the vertical axis and random scaling in the range $[0.7, 1.4]$. After random flipping and scaling, a random image crop of size 200×200 is also selected. The ResNet50 is imported from `torchvision.models` in PyTorch with the pretrained option set to true, all other network parameters are randomly initialized using the default initializer in PyTorch.

D.3. Prediction

For this experiment, we use a slight variation of Algorithm 1 in the paper, which is found in Algorithm S1. There, T is the number of gradient ascent iterations, λ is the stepsize, Ω_1 is an early-stopping threshold and Ω_2 is a degeneration tolerance. Following IoU-Net, we set $T = 5, \Omega_1 = 0.001$ and $\Omega_2 = -0.01$. Based on the validation set, we select $\lambda = 3$. We refine a single estimate \hat{y} , predicted by each baseline model.

D.4. Baselines

All baselines are trained for 75 epochs with a batch size of 32, using the ADAM optimizer with weight decay of 0.001. Identical data augmentation and parameter initialization as for our proposed model is used.

Direct The DNN architecture of *Direct* first extracts ResNet50 features $g_x \in \mathbb{R}^{2048}$ from the input image x . The feature vector g_x is then processed by two fully-connected layers ($2048 \rightarrow 2048, 2048 \rightarrow 1$), outputting the prediction $\hat{y} \in \mathbb{R}$. It is trained by minimizing either the Huber or L^2 loss.

Gaussian The Gaussian model is defined using a DNN $f_\theta(x)$ according to,

$$\begin{aligned} p(y|x; \theta) &= \mathcal{N}(y; \mu_\theta(x), \sigma_\theta^2(x)), \\ f_\theta(x) &= [\mu_\theta(x) \quad \log \sigma_\theta^2(x)]^\top \in \mathbb{R}^2. \end{aligned} \quad (\text{S3})$$

It is trained by minimizing the negative log-likelihood, corresponding to the loss,

$$J(\theta) = \frac{1}{n} \sum_{i=1}^n \frac{(y_i - \mu_\theta(x_i))^2}{\sigma_\theta^2(x_i)} + \log \sigma_\theta^2(x_i). \quad (\text{S4})$$

The DNN architecture of $f_\theta(x)$ first extracts ResNet50 features $g_x \in \mathbb{R}^{2048}$ from the input image x . The feature vector

Algorithm S1 Prediction via gradient-based refinement (variation)

Input: $x^*, \hat{y}, T, \lambda, \Omega_1, \Omega_2$.

- 1: $y \leftarrow \hat{y}$.
 - 2: **for** $t = 1, \dots, T$ **do**
 - 3: PrevValue $\leftarrow f_\theta(x^*, y)$.
 - 4: $y \leftarrow y + \lambda \nabla_y f_\theta(x^*, y)$.
 - 5: NewValue $\leftarrow f_\theta(x^*, y)$.
 - 6: **if** $|\text{PrevValue} - \text{NewValue}| < \Omega_1$ **or** $(\text{NewValue} - \text{PrevValue}) < \Omega_2$ **then**
 - 7: **Return** y .
 - 8: **Return** y .
-

g_x is then processed by two heads of two fully-connected layers (2048 \rightarrow 2048, 2048 \rightarrow 1) to output $\mu_\theta(x)$ and log $\sigma_\theta^2(x)$. The mean $\mu_\theta(x)$ is taken as the prediction \hat{y} .

Laplace The Laplace model is defined using a DNN $f_\theta(x)$ according to,

$$p(y|x; \theta) = \frac{1}{2\beta_\theta(x)} \exp\left\{-\frac{|y - \mu_\theta(x)|}{\beta_\theta(x)}\right\}, \quad (\text{S5})$$
$$f_\theta(x) = [\mu_\theta(x) \quad \log \beta_\theta(x)]^\top \in \mathbb{R}^2.$$

It is trained by minimizing the negative log-likelihood, corresponding to the loss,

$$J(\theta) = \frac{1}{n} \sum_{i=1}^n \frac{|y_i - \mu_\theta(x_i)|}{\beta_\theta(x_i)} + \log \beta_\theta(x_i). \quad (\text{S6})$$

The DNN architecture of $f_\theta(x)$ first extracts ResNet50 features $g_x \in \mathbb{R}^{2048}$ from the input image x . The feature vector g_x is then processed by two heads of two fully-connected layers (2048 \rightarrow 2048, 2048 \rightarrow 1) to output $\mu_\theta(x)$ and log $\beta_\theta(x)$. The mean $\mu_\theta(x)$ is taken as the prediction \hat{y} .

Softmax The DNN architecture of *Softmax* first extracts ResNet50 features $g_x \in \mathbb{R}^{2048}$ from the input image x . The feature vector g_x is then processed by two fully-connected layers (2048 \rightarrow 2048, 2048 $\rightarrow C$), outputting logits for $C = 101$ discretized classes $\{0, 1, \dots, 100\}$. It is trained by minimizing either the cross-entropy (CE) and L^2 losses, $J = J_{CE} + 0.1J_{L^2}$, or the CE, L^2 and variance [47] losses, $J = J_{CE} + 0.1J_{L^2} + 0.05J_{Var}$. The prediction \hat{y} is computed as the softmax expected value.

D.5. Full results

Full experiment results, extending the results found in Table 3 (Section 4.3 in the paper), are provided in Table S1.

Appendix E. Head-pose estimation

In this appendix, further details on the head-pose estimation experiments (Section 4.4 in the paper) are provided.

Method	MAE
Niu et al. [46]	5.74 \pm 0.05
Cao et al. [3]	5.47 \pm 0.01
Direct - Huber	4.80 \pm 0.06
Direct - Huber + Refinement	4.74 \pm 0.06
Direct - L2	4.81 \pm 0.02
Direct - L2 + Refinement	4.65 \pm 0.02
Gaussian	4.79 \pm 0.06
Gaussian + Refinement	4.66 \pm 0.04
Laplace	4.85 \pm 0.04
Laplace + Refinement	4.81 \pm 0.04
Softmax - CE & L2	4.78 \pm 0.05
Softmax - CE & L2 + Refinement	4.65 \pm 0.04
Softmax - CE, L2 & Var	4.81 \pm 0.03
Softmax - CE, L2 & Var + Refinement	4.69 \pm 0.03

Table S1: Full results for the age estimation experiments. Gradient-based refinement using our proposed method consistently improves MAE (lower is better) for the age predictions outputted by a number of baselines.

E.1. Network architecture

The DNN architecture $f_\theta(x, y)$ of our proposed model first extracts ResNet50 features $g_x \in \mathbb{R}^{2048}$ from the input image x . The pose $y \in \mathbb{R}^3$ is processed by four fully-connected layers (dimensions: 3 \rightarrow 16, 16 \rightarrow 32, 32 \rightarrow 64, 64 \rightarrow 128), generating $g_y \in \mathbb{R}^{128}$. The two feature vectors g_x, g_y are then concatenated to form $g_{x,y} \in \mathbb{R}^{2048+128}$, which is processed by two fully-connected layers (2048 + 128 \rightarrow 2048, 2048 \rightarrow 1), outputting $f_\theta(x, y) \in \mathbb{R}$.

E.2. Training

Our model is trained using $M = 1024$ samples from a proposal distribution $q(y|y_i)$ (Eq. 5 in the paper) with $L = 2$ and variances $\sigma_1^2 = 1^2$, $\sigma_2^2 = 20^2$ for Yaw, Pitch and Roll. It is trained for 75 epochs with a batch size of 32, using the ADAM optimizer with weight decay of 0.001. The images x are of size 64×64 . For data augmentation, we use random flipping along the vertical axis and random scaling in the range $[0.7, 1.4]$. After random flipping and scaling, a

random image crop of size 64×64 is also selected. The ResNet50 is imported from `torchvision.models` in PyTorch with the pretrained option set to true, all other network parameters are randomly initialized using the default initializer in PyTorch.

E.3. Prediction

For this experiment, we also use the prediction procedure detailed in Algorithm S1. Again following IoU-Net, we set $T = 5$, $\Omega_1 = 0.001$ and $\Omega_2 = -0.01$. Based on the validation set, we select $\lambda = 0.1$. We refine a single estimate \hat{y} , predicted by each baseline model.

E.4. Baselines

All baselines are trained for 75 epochs with a batch size of 32, using the ADAM optimizer with weight decay of 0.001. Identical data augmentation and parameter initialization as for our proposed model is used.

Direct The DNN architecture of *Direct* first extracts ResNet50 features $g_x \in \mathbb{R}^{2048}$ from the input image x . The feature vector g_x is then processed by two fully-connected layers ($2048 \rightarrow 2048$, $2048 \rightarrow 3$), outputting the prediction $\hat{y} \in \mathbb{R}^3$. It is trained by minimizing either the Huber or L^2 loss.

Gaussian The Gaussian model is defined using a DNN $f_\theta(x)$ according to,

$$\begin{aligned} p(y|x; \theta) &= \mathcal{N}(y; \mu_\theta(x), \Sigma_\theta(x)), \quad \Sigma_\theta(x) = \text{diag}(\sigma_\theta^2(x)), \\ y &= [y_1 \quad y_2 \quad y_3]^\top \in \mathbb{R}^3, \\ \mu_\theta(x) &= [\mu_{1,\theta}(x) \quad \mu_{2,\theta}(x) \quad \mu_{3,\theta}(x)]^\top \in \mathbb{R}^3, \\ \sigma_\theta^2(x) &= [\sigma_{1,\theta}^2(x) \quad \sigma_{2,\theta}^2(x) \quad \sigma_{3,\theta}^2(x)]^\top \in \mathbb{R}^3, \\ f_\theta(x) &= [\mu_\theta(x)^\top \quad \log \sigma_\theta^2(x)^\top]^\top \in \mathbb{R}^6. \end{aligned} \tag{S7}$$

It is trained by minimizing the negative log-likelihood, corresponding to the loss,

$$J(\theta) = \frac{1}{n} \sum_{i=1}^n \left(\sum_{k=1}^3 \frac{(y_{k,i} - \mu_{k,\theta}(x_i))^2}{\sigma_{k,\theta}^2(x_i)} + \log \sigma_{k,\theta}^2(x_i) \right). \tag{S8}$$

The DNN architecture of $f_\theta(x)$ first extracts ResNet50 features $g_x \in \mathbb{R}^{2048}$ from the input image x . The feature vector g_x is then processed by two heads of two fully-connected layers ($2048 \rightarrow 2048$, $2048 \rightarrow 3$) to output $\mu_\theta(x) \in \mathbb{R}^3$ and $\log \sigma_\theta^2(x) \in \mathbb{R}^3$. The mean $\mu_\theta(x)$ is taken as the prediction \hat{y} .

Laplace Following [17], the Laplace model is defined using a DNN $f_\theta(x)$ according to,

$$\begin{aligned} p(y|x; \theta) &= \prod_{k=1}^3 \beta_{k,\theta}(x)^{-\frac{1}{2}} \exp\left\{-\frac{1}{2} \left(\sum_{k=1}^3 \frac{(y_k - \mu_{k,\theta}(x))^2}{\beta_{k,\theta}(x)} \right)^{\frac{1}{2}}\right\}, \\ y &= [y_1 \quad y_2 \quad y_3]^\top \in \mathbb{R}^3, \\ \mu_\theta(x) &= [\mu_{1,\theta}(x) \quad \mu_{2,\theta}(x) \quad \mu_{3,\theta}(x)]^\top \in \mathbb{R}^3, \\ \beta_\theta(x) &= [\beta_{1,\theta}(x) \quad \beta_{2,\theta}(x) \quad \beta_{3,\theta}(x)]^\top \in \mathbb{R}^3, \\ f_\theta(x) &= [\mu_\theta(x)^\top \quad \log \beta_\theta(x)^\top]^\top \in \mathbb{R}^6. \end{aligned} \tag{S9}$$

It is trained by minimizing the negative log-likelihood, corresponding to the loss,

$$J(\theta) = \frac{1}{n} \sum_{i=1}^n \left\{ \left(\sum_{k=1}^3 \frac{(y_{k,i} - \mu_{k,\theta}(x_i))^2}{\beta_{k,\theta}(x_i)} \right)^{\frac{1}{2}} + \sum_{k=1}^3 \log \beta_{k,\theta}(x_i) \right\}. \tag{S10}$$

The DNN architecture of $f_\theta(x)$ first extracts ResNet50 features $g_x \in \mathbb{R}^{2048}$ from the input image x . The feature vector g_x is then processed by two heads of two fully-connected layers ($2048 \rightarrow 2048$, $2048 \rightarrow 3$) to output $\mu_\theta(x) \in \mathbb{R}^3$ and $\log \beta_\theta(x) \in \mathbb{R}^3$. The mean $\mu_\theta(x)$ is taken as the prediction \hat{y} .

Softmax The DNN architecture of *Softmax* first extracts ResNet50 features $g_x \in \mathbb{R}^{2048}$ from the input image x . The feature vector g_x is then processed by three heads of two fully-connected layers ($2048 \rightarrow 2048$, $2048 \rightarrow C$), outputting logits for $C = 151$ discretized classes $\{-75, -74, \dots, 75\}$ for the Yaw, Pitch and Roll angles (in degrees). It is trained by minimizing either the cross-entropy (CE) and L^2 losses, $J = J_{CE} + 0.1J_{L^2}$, or the CE, L^2 and variance [47] losses, $J = J_{CE} + 0.1J_{L^2} + 0.05J_{Var}$. The prediction \hat{y} is obtained by computing the softmax expected value for Yaw, Pitch and Roll.

E.5. Full results

Full experiment results, extending the results found in Table 4 (Section 4.4 in the paper), are provided in Table S2.

Method	Yaw MAE	Pitch MAE	Roll MAE	Average MAE
Yang et al. [65]	4.24	4.35	4.19	4.26
Gu et al. [19]	3.91	4.03	3.03	3.66
Yang et al. [64]	2.89	4.29	3.60	3.60
Direct - Huber	2.78 ± 0.09	3.73 ± 0.13	2.90 ± 0.09	3.14 ± 0.07
Direct - Huber + Refinement	2.75 ± 0.08	3.70 ± 0.11	2.87 ± 0.09	3.11 ± 0.06
Direct - L2	2.81 ± 0.08	3.60 ± 0.14	2.85 ± 0.08	3.09 ± 0.07
Direct - L2 + Refinement	2.78 ± 0.08	3.62 ± 0.13	2.81 ± 0.08	3.07 ± 0.07
Gaussian	2.89 ± 0.09	3.64 ± 0.13	2.83 ± 0.09	3.12 ± 0.08
Gaussian + Refinement	2.84 ± 0.08	3.67 ± 0.12	2.81 ± 0.08	3.11 ± 0.07
Laplace	2.93 ± 0.08	3.80 ± 0.15	2.90 ± 0.07	3.21 ± 0.06
Laplace + Refinement	2.89 ± 0.07	3.81 ± 0.13	2.88 ± 0.06	3.19 ± 0.06
Softmax - CE & L2	2.73 ± 0.09	3.63 ± 0.13	2.77 ± 0.11	3.04 ± 0.08
Softmax - CE & L2 + Refinement	2.67 ± 0.08	3.61 ± 0.12	2.75 ± 0.10	3.01 ± 0.07
Softmax - CE, L2 & Var	2.83 ± 0.12	3.79 ± 0.10	2.84 ± 0.11	3.15 ± 0.07
Softmax - CE, L2 & Var + Refinement	2.76 ± 0.10	3.74 ± 0.09	2.83 ± 0.10	3.11 ± 0.06

Table S2: Full results for the head-pose estimation experiments. Gradient-based refinement using our proposed method consistently improves the average MAE for Yaw, Pitch, Roll (lower is better) for the predicted poses outputted by a number of baselines.